Journal of Hydraulic Research Vol. 43, No. 4 (2005), pp. 339–350

Finite volume modeling of variable density shallow-water flow equations for a well-mixed estuary: application to the Río Maipo estuary in central Chile

Modèle en volumes finis des équations d'un écoulement en eau peu profonde de densité variable dans un estuaire bien mélangé: application à l'estuaire de Río Maipo au centre du Chili

L. BRICE, *Waterscience Research Community, 728 Matsonia Dr., Foster City, CA 94404, USA. E-mail: brice@watersci.org*

C. YARKO NIÑO, Associate Professor, *Department of Civil Engineering, University of Chile, Casilla 228-3, Santiago, Chile. Tel.: (56) 2 696-8448; fax: (56) 2 689-4171; e-mail: ynino@cec.uchile.cl*

M. CRISTIAN ESCAURIAZA, *School of Civil and Environmental Engineering, Georgia Institute of Technology, GA, USA. E-mail: cristian.escauriaza@ce.gatech.edu*

ABSTRACT
Strong advective flows in well-mixed estuaries can produce abrupt fronts and density gradients, which cause secondary circulation and affect the ecosystem by generating recirculation or accumulation of pollutants inside the estuary. To model these complex phenomena, a method capable of adequately representing the dynamics of the flow by considering the salt as an active tracer, influencing the transport within the estuary, is required. A numerical model based on the finite volume MUSCL-Hancock method is used to solve the shallow-water flow equations in combination with an advection/diffusion of salt equation, to simulate two-dimensional unsteady flow in a vertically well-mixed estuary. The salt transport equation is coupled to the momentum equations via the hydrostatic term, which permits simulation of baroclinic secondary circulation. A series of benchmark test problems are used to validate the model and demonstrate its capabilities. The model is then used to simulate the saline intrusion within the Río Maipo estuary, a well-mixed tidal river in central Chile. The numerical results predict that the presence of a littoral bar at the river mouth precludes the upstream transport of salt, resulting in an almost negligible salinity intrusion in the system. This result is validated with field measurements of salinity, taken from within the estuary.

RÉSUMÉ
Les écoulements convectifs forts dans les estuaires bien mélangés peuvent produire des fronts raides et les gradients de densité à l'origine de circulations secondaires et affectant l'écosystème en produisant des recyclages ou des accumulations des polluants à l'intérieur de l'estuaire. Pour modéliser ces phénomènes complexes, une méthode capable de représenter de façon adéquate la dynamique de l'écoulement en considérant le sel comme traceur actif, influençant le transport dans l'estuaire, est nécessaire. Le modèle numérique basé sur la méthode des volumes finis MUSCL-Hancock est utilisé pour résoudre les équations d'un écoulement en eau peu profonde combinées avec l'équation d'advection/diffusion de sel, pour simuler l'écoulement instationnaire bidimensionnel dans un estuaire verticalement bien mélangé. L'équation de transport de sel est couplée aux équations dynamiques par le terme hydrostatique, ce qui permet la simulation de la circulation secondaire barocline . Une série de problèmes test ont servi de benchmark pour valider le modèle et démontrer ses possibilités. Le modèle a été utilisé ensuite pour simuler l'intrusion saline dans le Río Estuaire de Maipo, un fleuve à marée bien mélangé au centre du Chili. Les résultats numériques prévoient que la présence d'une barre littorale à l'embouchure du fleuve empêche le transport du sel vers l'amont, rendant négligeable l'intrusion de salinité dans le système. Ce résultat est validé par des mesures de salinité effectuées dans l'estuaire.

Keywords: Well-mixed estuary, baroclinic flow, Río Maipo, MUSCL-Hancock solution, saline intrusion.

1 Introduction

Flow in estuaries and the coastal sea is distinguished by the myriad of residual circulation patterns that occur product of the net barotropic and baroclinic gradients that establish themselves at subtidal frequencies. Vertically well-mixed estuaries are characterized by negligible vertical gradients of salt concentration throughout the water column compared to corresponding horizontal gradients. This pattern of saline heterogeneity can lead to secondary currents flowing transverse to the dominant flow, and currents that advect salt upstream, contrary to the net direction of flow in the system. Often the baroclinic upstream advection is the process that balances turbulent salt diffusion and maintains the net salt balance in an estuary (Dyer, 1997).

The Río Maipo estuary is a vertically well-mixed microtidal estuary, which discharges into the Pacific just south of the Port of San Antonio, Chile. The mean annual discharge is 90 m^3/s, with highest discharge occurring during the winter rains from June

Revision received March 3, 2003 / Open for discussion until May 31, 2006.

through September. Strong coastal wave activity and open shoreline combine to restrict flow at the rivermouth by the formation of an extensive littoral bar. The Maipo is a shallow estuary with a mean depth of about 1.4 ± 0.4 m and a mean top width of about 250 m. The Maipo is characterized by strong advective flows and the presence of potentially abrupt density fronts at the interface between seawater and freshwater. Interest in the hydrodynamics has arisen from an interest in both sediment dynamics and water quality within the estuary and the coastal sea. The Maipo catchment is home to the entire metropolitan region of Santiago de Chile as well as copper mining in the Andes and considerable agriculture in the western catchment. Growth in the city's outlying suburbs has caused concern about both particulate and trace metal contamination of the lower portion of the river.

To begin the study of the circulation dynamics of an estuary like the Maipo, a hydrodynamic model was needed that would be simple to implement and modify, precise in its resolution of fronts and steep gradients, and capable of reproducing the pressure gradient effects produced by horizontal gradients in density. Examples of the importance of density dependent pressure effects in estuarine simulations can be observed in a 3-D simulation of the Ria de Pontevedra, Spain (Ruiz-Villareal *et al*., 2002) and in Gross *et al*. (1999) who found that baroclinic effects were necessary to reproduce in both a three-dimensional and a well-mixed model in order to simulate the net salt flux into South San Francisco Bay.

The shallow-water set of equations has been widely implemented recently thanks to the advancement of a set of numerical techniques based on the linear or quasi-linear properties of hyperbolic conservation laws. Integration of these conservation laws in the finite volume method (FVM) has become a popular solution to many environmental flows including the complex intermittently flooded flow within floodplain networks and irrigation canals (Zhao *et al*., 1994), and detailed reproduction of dam failures (Valiani *et al*., 2002). Recent developments have seen the methods refined to include arbitrary morphology using structured and unstructured FVM geometries and adaptive meshing schemes to resolve flow around complex geometry (Sleigh *et al*., 1998). Improvements have also been made to integrate the bed slope and friction slope source terms as well as the pressure acting outside of each FVM cell (Bradford and Sanders, 2002; Valiani *et al*., 2002). Indeed, these methods can boast both a maturity and acceptance in their application to many shallow-water flow situations.

Capitalizing on these advances, this research uses the shallow-water flow conception to construct a two-dimensional hydrodynamic model of a well-mixed estuary that is capable of resolving flow over arbitrary topography using non-orthogonal FVM cells. However, given the effect of salt on the horizontal momentum balance it was necessary to treat salt not as a passive tracer, but as a variable in the momentum conservation. This was achieved by applying the Boussinesq approximation to preserve the density effects in the hydrostatic pressures terms. The formulation still grants the approximation of the conservation laws as hyperbolic and thus quasi-linear, which permits a robust simulation of the horizontal flow dynamics, while preserving the efficiency of a characteristic method. The numerical method used to solve the equations was the MUSCL-Hancock method, one of the Godunov-type methods, as described by Toro (1997); the solution is both second-order accurate and conforms to the Total Variance Diminishing criterion when used with a slope-limiting function (Hirsch, 1988). In this paper the method is briefly described and five "benchmark" test problems are represented, which serve to validate the proper coding of the solution and demonstrate the capability of the model to handle a variety of flow conditions. The model is finally applied to the Río Maipo for a 4-day simulation whose primary objective is to compare with field measurements and thus draw conclusions about the intrusion dynamics inside the rivermouth. A subsequent paper will present a detailed description of both field measurements and simulations of the Río Maipo estuary that depict the potential for morphological variability at the rivermouth and emphasize the important role of rivermouth morphodynamics in controlling up-estuary salt flux.

2 Numerical model

2.1 Governing equations

The conservation equations for the estuary problem are a variation of the St. Venant equations; the hydrostatic approximation is made, which eliminates the variability in the vertical direction. The Boussinesq approximation is used to reproduce the effect of variable water density on the momentum balance while preserving the incompressibility assumption. The four mass, momentum, and salt conservation laws can be written as,

$$U_t + [F(U)]_x + [G(U)]_y = H(U), \tag{1}$$

with vectors U, F, G, and H given by:

$$U = \begin{pmatrix} h \\ uh \\ vh \\ \rho h \end{pmatrix}, \quad F(U) = \begin{pmatrix} uh \\ u^2 h + \dfrac{g}{2\rho_0}\rho h^2 \\ uvh \\ \rho uh - hD_x \dfrac{\partial \rho}{\partial x} \end{pmatrix},$$

$$G(U) = \begin{pmatrix} vh \\ vuh \\ v^2 h + \dfrac{g}{2\rho_0}\rho h^2 \\ \rho vh - hD_y \dfrac{\partial \rho}{\partial y} \end{pmatrix}, \tag{2}$$

$$H(U) = \begin{pmatrix} 0 \\ -\dfrac{g}{\rho_0}\rho h (z_b)_x - \dfrac{1}{\rho_0}\tau_{bx} \\ -\dfrac{g}{\rho_0}\rho h (z_b)_y - \dfrac{1}{\rho_0}\tau_{by} \\ 0 \end{pmatrix},$$

The notation $()_{x_i}$ is shorthand for the partial derivative $\partial/\partial x_i$. The variable h represents the height of the water column over the variable bed elevation z_b, while the local instantaneous depth-averaged velocities along the x and y coordinates of the planar surface are u and v, respectively. The local instantaneous water density is expressed as ρ, and ρ_0 is the freshwater reference density. The dispersion coefficients, D_x, and D_y are estimated using

Elder's relation (Fischer *et al*., 1979), and the shear stress, τ_b, is calculated using a zero-order closure relation that employs Manning's coefficient (Valiani *et al*., 2002),

$$\tau_{bx} = \frac{\rho g h}{h^{4/3}} n^2 u\sqrt{u^2+v^2}, \quad \tau_{by} = \frac{\rho g h}{h^{4/3}} n^2 v\sqrt{u^2+v^2} \tag{3}$$

Equation (1) can be written in quasi-linear form as,

$$U_t + AU_x + BU_y = H, \tag{4}$$

The eigenvalues of the two Jacobian matrices, A and B, in Eq. (4) are, respectively,

$$\begin{aligned} \delta &= [u + \sqrt{\rho/\rho_0 g h},\ u - \sqrt{\rho/\rho_0 g h},\ u,\ u], \\ \omega &= [v + \sqrt{\rho/\rho_0 g h},\ v - \sqrt{\rho/\rho_0 g h},\ v,\ v] \end{aligned} \tag{5}$$

The eigenvalues are used to generate the Godunov approximation of the Jacobians as matrices of constant coefficients; this is done to calculate the Riemann flux (Toro, 1997).

2.2 *MUSCL-Hancock method*

The conservation equations are solved on a finite volume grid of non-orthogonal quadrilaterals using the MUSCL-Hancock method. The method is described here with special focus on the adaptations made to resolve the advection and diffusion of salt. For a more complete presentation of the MUSCL-Hancock method please refer to Toro (1997, 2001) and to Bradford and Katopodes (1999), Bradford and Sanders (2002), and Bradford *et al*. (1997).

The method will be described in five steps with reference to a quadrilateral identified by the four vertices (A, B, C, D) (Fig. 1). The cell face between vertices A and B will be used to illustrate what is performed at each of the four cell faces. The primitive equations are first transformed to a local coordinate grid using,

$$\frac{\partial}{\partial x} = \xi_x \frac{\partial}{\partial \xi} + \eta_x \frac{\partial}{\partial \eta}, \quad \frac{\partial}{\partial y} = \xi_y \frac{\partial}{\partial \xi} + \eta_y \frac{\partial}{\partial \eta} \tag{6}$$

where ξ and η are the local coordinates between adjacent cell-centroids ($C_{i,j}$). The primitive equations are used to generate a solution during the Predictor steps. Afterwards, the conservative form of (1) is solved by calculating the local 1-D boundary integrals to compute the spatial derivatives. Applying Green's theorem of integration by parts, the discrete integral form of (1) can be written as,

$$\frac{\partial}{\partial t} U_{i,j}\Omega_{i,j} + \sum_{\text{ABCD}} (\vec{F}^I \cdot \vec{S}) = H_{i,j}\Omega_{i,j} \tag{7}$$

where the vector $\vec{F}^I$ is the projection of the fluxes F and G, onto each of the four cell faces, and $\Omega_{i,j}$ is the area of the cell under consideration.

Step 1. Gradient calculation: The slope-limited gradients are calculated using the MINBEE averaging function, whose primary purpose is to diminish the order of the calculation in the region of sharp gradients in order to avoid oscillations (Toro, 1997). Using the primitive form of (1), the primitive variables W ($W = [huv\rho]^{\mathrm{T}}$) are evolved forward by one-half time step (Bradford and Katopodes, 1999). As such, the discrete continuity and momentum equations are,

$$\begin{aligned} h_{i,j}^{n+1/2} &= h_{i,j}^n - \frac{\Delta t}{2}\left\{ u_\xi \frac{\overline{\Delta h}_\xi}{\Delta \xi} + u_\eta \frac{\overline{\Delta h}_\eta}{\Delta \eta} \right. \\ &\qquad \left. + h\left(\xi_x \frac{\overline{\Delta u}_\xi}{\Delta \xi} + \xi_y \frac{\overline{\Delta v}_\xi}{\Delta \xi} + \eta_x \frac{\overline{\Delta u}_\eta}{\Delta \eta} + \eta_y \frac{\overline{\Delta v}_\eta}{\Delta \eta} \right) \right\}_{i,j} \end{aligned}$$

$$\begin{aligned} u_{i,j}^{n+1/2} &= u_{i,j}^n - \frac{\Delta t}{2}\left\{ u_\xi \frac{\overline{\Delta u}_\xi}{\Delta \xi} + u_\eta \frac{\overline{\Delta u}_\eta}{\Delta \eta} + \frac{g}{\rho_0}\left[\rho\left(\xi_x \frac{\overline{\Delta \zeta}_\xi}{\Delta \xi} + \eta_x \frac{\overline{\Delta \zeta}_\eta}{\Delta \eta} \right) \right.\right. \\ &\qquad \left.\left. + \frac{h}{2}\left(\xi_x \frac{\overline{\Delta \rho}_\xi}{\Delta_\xi} + \eta_x \frac{\overline{\Delta \rho}_\eta}{\Delta \eta} \right) \right] \right\}_{i,j} - \frac{\Delta t}{2}\left\{ \frac{g\rho}{h^{4/3}} n^2 u\sqrt{u^2+v^2} \right\}_{i,j} \end{aligned}$$

$$\begin{aligned} v_{i,j}^{n+1/2} &= v_{i,j}^n - \frac{\Delta t}{2}\left\{ u_\xi \frac{\overline{\Delta v}_\xi}{\Delta \xi} + u_\eta \frac{\overline{\Delta v}_\eta}{\Delta \eta} + \frac{g}{\rho_0}\left[\rho\left(\xi_y \frac{\overline{\Delta \zeta}_\xi}{\Delta \xi} + \eta_y \frac{\overline{\Delta \zeta}_\eta}{\Delta \eta} \right) \right.\right. \\ &\qquad \left.\left. + \frac{h}{2}\left(\xi_y \frac{\overline{\Delta \rho}_\xi}{\Delta_\xi} + \eta_y \frac{\overline{\Delta \rho}_\eta}{\Delta \eta} \right) \right] \right\}_{i,j} - \frac{\Delta t}{2}\left\{ \frac{g\rho}{h^{4/3}} n^2 v\sqrt{u^2+v^2} \right\}_{i,j} \end{aligned} \tag{8}$$

where the terms $\overline{\Delta W}_{i,j}$ are the slope-limited gradients of the primitive variables, $\Delta\xi$ and $\Delta\eta$ are the radial distances between $C_{i,j}$ and the adjacent centroids $C_{i+1,j}$ and $C_{i,j+1}$, respectively, the coefficients ξ_x, ξ_y, η_x, and η_y are the metrics of the generalized coordinate system (Fig. 1). The term ζ is the water surface height above the datum ($\zeta = h + z_b$), and n is the Manning friction coefficient. The second order terms in the salt conservation equation require an extra step in the discretization. First, the outer derivative is taken as a finite-difference at the cell face then the inner derivative is zero-order extrapolated from the adjacent cell centroid. An upwind criterion is used to choose the adjacent centroid; that is, the centroid that is upstream is extrapolated to the face that is downstream of it. For example, the term

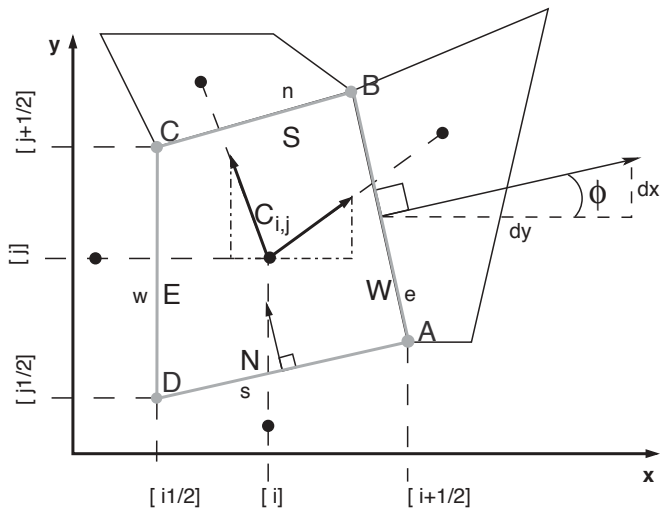

Figure 1 Non-orthogonal quadrilateral FVM cell used to develop the MUSCL solution.

$\{\xi_x \partial/\partial\xi(\xi_x h \partial\rho/\partial\xi)\}_{i,j}$ is discretized across the cell centroid as,

$$\xi_x \frac{\partial}{\partial\xi}\left(\xi_x h \frac{\partial\rho}{\partial\xi}\right) = \frac{\xi_x^2}{\Delta\xi}\left\{\left(h\frac{\Delta\rho}{\Delta\xi}\right)_{i+1/2,j} - \left(h\frac{\Delta\rho}{\Delta\xi}\right)_{i-1/2,j}\right\} \tag{9}$$

Afterwards, the interior gradients are substituted for the slope-limited gradients from the upstream cell centroid,

$$\begin{aligned}&\frac{\xi_x^2}{\Delta\xi}\left\{\left(h\frac{\Delta\rho}{\Delta\xi}\right)_{i+1/2,j} - \left(h\frac{\Delta\rho}{\Delta\xi}\right)_{i-1/2,j}\right\}\\ &\quad= \begin{cases} \frac{\xi_x^2}{\Delta\xi^2}\left\{\left(h\overline{\Delta\rho}_\xi\right)_{i,j} - \left(h\overline{\Delta\rho}_\xi\right)_{i-1,j}\right\}, & u > 0\\ \frac{\xi_x^2}{\Delta\xi^2}\left\{\left(h\overline{\Delta\rho}_\xi\right)_{i+1,j} - \left(h\overline{\Delta\rho}_\xi\right)_{i,j}\right\}, & u < 0\end{cases}\end{aligned} \tag{10}$$

In this way the eight second-order terms in the salt conservation equation are calculated. As an example if both u and v are > 0, then the salt conservation equation would be,

$$\begin{aligned}\rho_{i,j}^{n+1/2} = \rho_{i,j}^{n} &- \frac{\Delta t}{2}\left\{u_\xi\frac{\overline{\Delta\rho}_\xi}{\Delta_\xi} + u_\eta\frac{\overline{\Delta\rho}_\eta}{\Delta\eta}\right\}_{i,j}\\ &- \frac{\Delta t}{2}\left\{\frac{D_x}{h_{i,j}}\frac{\xi_x^2}{\Delta\xi^2}\left[\left(h\overline{\Delta\rho}_\xi\right)_{i,j} - \left(h\overline{\Delta\rho}_\xi\right)_{i-1,j}\right]\right.\\ &\left.+ \frac{D_x}{h_{i,j}}\frac{\xi_x\eta_x}{\Delta\xi\Delta\eta}\left[\left(h\overline{\Delta\rho}_\xi\right)_{i,j} - \left(h\overline{\Delta\rho}_\xi\right)_{i-1,j}\right]\right\}\\ &- \frac{\Delta t}{2}\left\{\frac{D_x}{h_{i,j}}\frac{\eta_x\xi_x}{\Delta\eta\Delta\xi}\left[\left(h\overline{\Delta\rho}_\xi\right)_{i,j} - \left(h\overline{\Delta\rho}_\xi\right)_{i,j-1}\right]\right.\\ &\left.+ \frac{D_x}{h_{i,j}}\frac{\eta_x^2}{\Delta\eta^2}\left[\left(h\overline{\Delta\rho}_\eta\right)_{i,j} - \left(h\overline{\Delta\rho}_\eta\right)_{i,j-1}\right]\right\}\\ &- \frac{\Delta t}{2}\left\{\frac{D_y}{h_{i,j}}\frac{\xi_y^2}{\Delta\xi^2}\left[\left(h\overline{\Delta\rho}_\xi\right)_{i,j} - \left(h\overline{\Delta\rho}_\xi\right)_{i-1,j}\right]\right.\\ &\left.+ \frac{D_y}{h_{i,j}}\frac{\xi_y\eta_y}{\Delta\xi\Delta\eta}\left[\left(h\overline{\Delta\rho}_\eta\right)_{i,j} - \left(h\overline{\Delta\rho}_\eta\right)_{i-1,j}\right]\right\}\\ &- \frac{\Delta t}{2}\left\{\frac{D_y}{h_{i,j}}\frac{\eta_y\xi_y}{\Delta\eta\Delta\xi}\left[\left(h\overline{\Delta\rho}_\xi\right)_{i,j} - \left(h\overline{\Delta\rho}_\xi\right)_{i,j-1}\right]\right.\\ &\left.+ \frac{D_y}{h_{i,j}}\frac{\eta_y^2}{\Delta\eta^2}\left[\left(h\overline{\Delta\rho}_\eta\right)_{i,j} - \left(h\overline{\Delta\rho}_\eta\right)_{i,j-1}\right]\right\}\end{aligned} \tag{11}$$

Step 2. Data reconstruction: Using the limited gradients $(\overline{\Delta W}_{i,j})$, the primitive variables are extrapolated from the centroids to each of the four cell faces (Fig. 1) as,

$$\begin{aligned}W_{i,j}^E &= W_{i,j}^{n+1/2} - \tfrac{1}{2}\left(\overline{\Delta W}_{i,j}\right)_\xi, \quad W_{i,j}^N = W_{i,j}^{n+1/2} - \tfrac{1}{2}\left(\overline{\Delta W}_{i,j}\right)_\eta,\\ W_{i,j}^W &= W_{i,j}^{n+1/2} + \tfrac{1}{2}\left(\overline{\Delta W}_{i,j}\right)_\xi, \quad W_{i,j}^S = W_{i,j}^{n+1/2} + \tfrac{1}{2}\left(\overline{\Delta W}_{i,j}\right)_\eta,\end{aligned} \tag{12}$$

and then used to reconstruct the conservative variables from (2) at each of the cell faces. By using Green's theorem, both the first and second order space derivatives in (1) can be calculated as boundary integrals (Hirsch, 1988). Given the physical nature of the second-order or diffusive terms, they are calculated in hyperbolic form, but separately from the advective fluxes (Sanders *et al.*, 2001; Sanders and Piasecki, 2002) such that the sum of the interfacial fluxes in (7) is the sum of the advective and diffusive fluxes,

$$\vec{F}^I = F_\perp^{\text{adv}} + F_\perp^{\text{dif}} \tag{13}$$

The local one-dimensional fluxes across each of the four cell faces in Fig. 1 are,

$$\begin{aligned}F_\perp^{\text{adv}} &= \begin{pmatrix} u_\perp h \\ u_\perp h u + \dfrac{g}{2\rho_0}\rho h^2\cos\phi \\ u_\perp h v + \dfrac{g}{2\rho_0}\rho h^2\sin\phi \\ u_\perp h\rho \end{pmatrix},\\ F_\perp^{\text{adv}} &= \begin{pmatrix} 0 \\ 0 \\ 0 \\ -D_x h\cos\phi\dfrac{\partial\rho}{\partial x} - D_y h\sin\phi\dfrac{\partial\rho}{\partial y} \end{pmatrix}\end{aligned} \tag{14}$$

where the term $u_\perp$ is the velocity perpendicular to the cell face and ϕ is the angle between the cell-face normal vector and the x-axis (Bradford and Katopodes, 1999) (Fig. 1).

Step 3. Riemann problem solution for advective flux: A modified version of the approximate Riemann solver of Roe is used. The Riemann problem for the advective flux across the face AB, $(F_{\text{AB}\perp}^{\text{adv}})$, is calculated from the reconstructed fluxes on each side of the face as,

$$F_{\text{AB}\perp}^{\text{adv}} = \tfrac{1}{2}\left[F_{\text{e}\perp}^{\text{adv}} + F_{\text{W}\perp}^{\text{adv}} - \kappa_{\text{AB}}(U_{\text{e}} - U_{\text{W}})\right] \tag{15}$$

The subscripts "e⊥" and "W⊥" denote the perpendicular fluxes on each side of the cell face AB; where "e" refers to extrapolation from the *adjacent* cell to the east of the cell face and "W" refers to the extrapolation from the cell *under consideration* to the west of the cell face (Fig. 1). Following the suggestion of Sanders (2001), Nujic's (1995) modified Lax-Friedrichs approximation for the Jacobian matrix of constant coefficients is used,

$$\kappa_{\text{AB}} = \max_{i,j}|\lambda_{\text{AB}}| \tag{16}$$

The term λ_{AB} is the vector of eigenvalues calculated using the Roe averaged primitive variables for the cell face AB,

$$\lambda_{\text{AB}} = \left[\hat{u}_\perp + \hat{a}, \hat{u}_\perp - \hat{a}, \hat{u}_\perp, \hat{u}_\perp\right]^{\text{T}} \tag{17}$$

here $\hat{a}$ is the density dependent shallow-water wave speed,

$$\hat{a} = \sqrt{\frac{\rho}{\rho_0}g\hat{h}}, \quad \hat{h} = \sqrt{h_{\text{e}}h_{\text{W}}} \tag{18}$$

and $\hat{h}$ denotes the Roe average of h.

Step 4. Diffusive flux calculation: The orthogonal gradients contained in the diffusive flux from (14) can be expressed in terms of the non-orthogonal coordinates ξ and η, and the gradient across the cell face is calculated from the values at the adjacent centroids,

$$\begin{aligned}\frac{\partial\rho}{\partial x} &= \xi_x\frac{\rho_{i+1,j} - \rho_{i,j}}{\Delta\xi} + \eta_x\frac{\rho_{i,j+1} - \rho_{i,j}}{\Delta\eta}\\ \frac{\partial\rho}{\partial y} &= \xi_y\frac{\rho_{i+1,j} - \rho_{i,j}}{\Delta\xi} + \eta_y\frac{\rho_{i,j+1} - \rho_{i,j}}{\Delta\eta}\end{aligned} \tag{19}$$

Finally, the advective and diffusive fluxes are combined using (13) and used to solve (7), the discrete form of the conservative equations in the Corrector step.

Step 5. Corrector step: The $n+1$ time step is gained by solving the discrete integral form of the conservation laws (Eq. 7),

$$U_{i,j}^{n+1} = U_{i,j}^{n} - \frac{\Delta t}{\Omega_{i,j}}\left(F_{\mathrm{AB}}^{I}\overline{\mathrm{AB}} + F_{\mathrm{BC}}^{I}\overline{\mathrm{BC}} - F_{\mathrm{CD}}^{I}\overline{\mathrm{CD}} - F_{\mathrm{DA}}^{I}\overline{\mathrm{DA}}\right) + \Delta t H_{i,j}^{n} \tag{20}$$

the terms $\overline{\mathrm{AB}}, \ldots, \overline{\mathrm{DA}}$ are the scalar lengths of the sides of the FVM cell $[i, j]$. The source term H includes the bed slope and friction slope terms,

$$H = \begin{pmatrix} 0 \\ -g\dfrac{\rho}{\rho_0}h\left(\dfrac{\partial z_b}{\partial x} + \dfrac{n^2}{h^{4/3}}u\sqrt{u^2+v^2}\right) \\ -g\dfrac{\rho}{\rho_0}h\left(\dfrac{\partial z_b}{\partial y} + \dfrac{n^2}{h^{4/3}}v\sqrt{u^2+v^2}\right) \\ 0 \end{pmatrix} \tag{21}$$

The bed slopes are evaluated via a centered difference and the friction slopes are calculated explicitly using the values from the time $n+1/2$, calculated in Step 1. The criterion for convergence is the same as for any Godunov-type method (Toro, 1997); no wave propagating within the domain may be allowed to travel a distance larger than Δx within a time Δt. The CFL restriction for non-orthogonal FVM cells can be written as,

$$\Delta t < \frac{\mathrm{CFL}\min\left[\left(\sqrt{\Delta\xi^2 + \Delta\eta^2}\right)_{i,j}\right]}{2\max\left[\left(\sqrt{u^2+v^2} + \sqrt{\rho/\rho_0 g h}\right)_{i,j}\right]} \tag{22}$$

where the max and min values are taken over the entire domain of elements $[i, j]$ (Valiani *et al.*, 2002).

2.3 Boundary conditions

The boundary conditions must be implemented in such a manner as to cause the appropriate behavior during the flux calculations. Fictitious cell centroids are generated outside the domain for the purpose of calculating boundary conditions at the cell face. For an impermeable boundary the perpendicular velocity ($u_\perp$) is null and the hydraulic head on both sides of the face must be equal to generate a null contribution to the Riemann flux. Given this condition the advective flux in (14) reduces to,

$$F_{\perp}^{\mathrm{adv}} = \left[0, \frac{g}{2\rho_0}\rho h^2 \cos\phi, \frac{g}{2\rho_0}\rho h^2 \sin\phi, 0\right]^{\mathrm{T}} \tag{23}$$

The scalar variables (ρ and h) can be estimated in the same manner as in the orthogonal case,

$$h_{\mathrm{g}} = h_{\mathrm{adj}}, \quad \Delta h_{\mathrm{g}} = -\Delta h_{\mathrm{adj}}, \quad \rho_{\mathrm{g}} = \rho_{\mathrm{adj}}, \quad \Delta\rho_{\mathrm{g}} = -\Delta\rho_{\mathrm{adj}} \tag{24}$$

where "g" refers to the value in the fictitious node and "adj" refers to the centroid adjacent to the fictitious node, within the domain.

At a flow boundary, the possibility of subcritical flow must be accounted for by extrapolating one variable from the domain. Either the velocity or water surface height can be extrapolated; the extrapolation is performed as an average between the adjacent FVM cell within the domain $[i, j]$ and an FVM cell upstream of, and adjacent to, cell $[i, j]$. That is,

$$W_{\mathrm{g}}^{k} = \frac{1}{2}\left(W_{\mathrm{adj}}^{k} + W_{\mathrm{adj}-1}^{k}\right) \tag{25}$$

where "adj − 1" refers to the cell adjacent to "adj" and upstream of it. Once the value of velocity or height has been extrapolated the other can be calculated via the continuity assumption. In the following sections the flow boundary conditions will be described for each particular problem presented.

3 Benchmarks

3.1 Partial dam breach

The partial dam breach has become a standard test problem for shock-capturing methods; examples can be found in Mingham and Causon (1998), Chaudhry (1993), and Sanders (2001) to name a few. This benchmark test demonstrates the capability of the model to resolve steep gradients (shock waves) as well as the backward propagating rarefaction wave and shear waves. A comparison is made with the finite-difference McCormack method presented in Chaudhry (1993). A dam wall separates a square domain into two equal halves; initially the water depth upstream is 10 m and downstream is 5 m, the velocity is zero everywhere and the water density is constant and equal to $1000\,\mathrm{kg/m^3}$. The simulation is frictionless and the solid boundary condition is implemented on the four sides of the box. The time series of water height shows a general agreement between the methods (Fig. 2, bottom). Initially, the MUSCL scheme indicates a steeper shock wave, but both methods converge near $t = 7$ s. Figure 3 shows a plot of the water surface at $t = 7.3$ s.

3.2 Damped propagation of a symmetric bore wave

This comparison is based on a test problem presented by Sobey (2002b). A one-dimensional disturbance propagates longitudinally along a prismatic canal of rectangular section $b_0 = 20$ m, area of flow $A_0 = 50\,\mathrm{m^2}$, and length $x_L = 5000$ m (Fig. 4). For more information about the analytical solution the reader is referred to Sobey (2002a,b). The wave propagation is not entirely free; Sobey (2002b) applies a constant friction factor, $\gamma = 10^{-3}\,\mathrm{s^{-1}}$ to the analytical solution; the same factor is applied

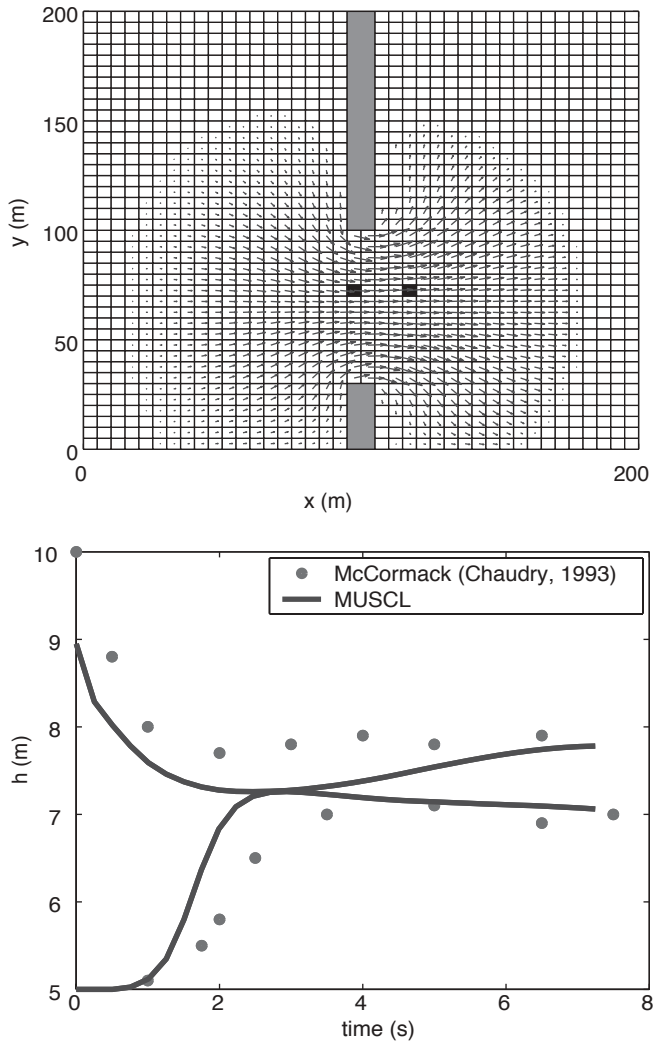

Figure 2 The 200 × 200 m^2 domain for dam breach simulation; arrows indicate velocity vectors greater than 0.1 m/s at $t = 7.3$ s after dam failure (top). The two black boxes indicate the cells presented in the time series on the right. Comparison of MUSCL solution with that given by the McCormack scheme presented in Chaudhry (1993) (bottom).

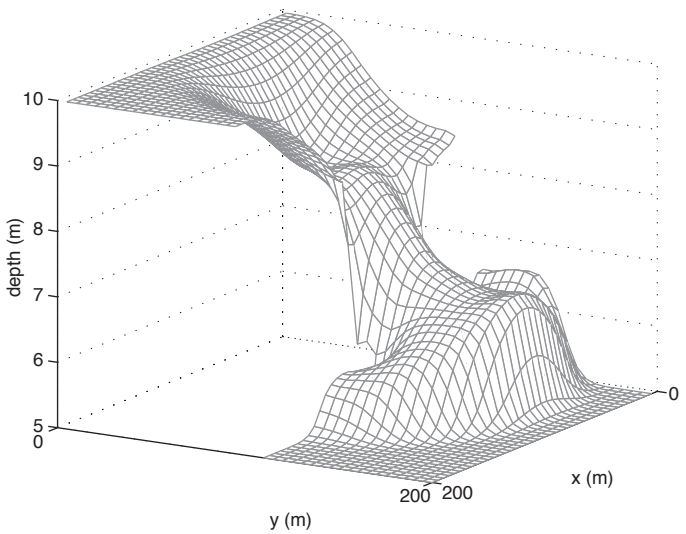

Figure 3 Water surface height at $t = 7.3$ s after dam failure.

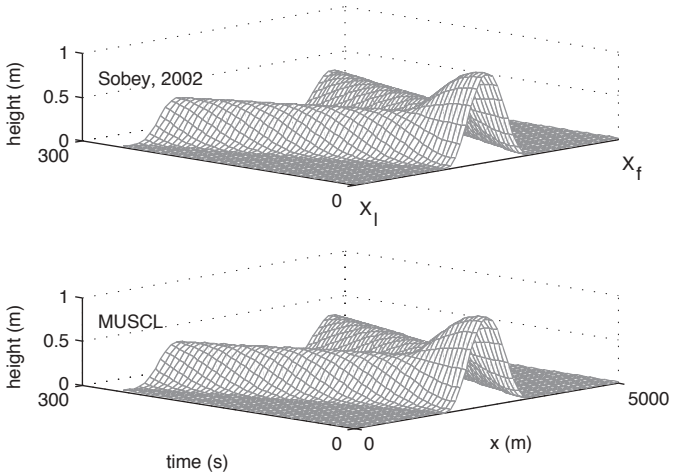

Figure 4 Propagation of a symmetric bore in a one-dimensional canal (Sobey, 2002a,b).

to the numerical solution. Initially, the water surface profile, z is,

$$z(x,0) = \begin{cases} \frac{1}{2}\left[1+\cos\left(\pi\frac{x-2500}{750}\right)\right] & \text{for } 1750 \le x \le 3250. \\ 0 & \text{otherwise} \end{cases} \tag{26}$$

The canal is discretized into 50 × 1 rectangular FVM elements; the boundary conditions were those of the solid wall, but the bore interaction with the canal boundaries was not studied.

As seen in Fig. 5, the MUSCL solution of the bore wave presents a slight asymmetry from front to back, as compared with the analytical solution, but there is substantial agreement between the wave fronts and the following troughs.

3.3 Steady-state flow in a convergent canal

This test is meant to demonstrate the capability of the model to handle non-orthogonal domains, as well as the conservative nature of the FVM solution. A steady flow of $Q = 10\,\text{m}^3/\text{s}$ of a homogeneous fluid with density $1000\,\text{kg/m}^3$, flows through a canal of rectangular section and convergent walls. As shown in Fig. 6, the width of the inflow section is $b_a = 50$ m and that of the outflow section is $b_b = 25$ m; the bed slope is 0.0001 from the inflow to the outflow. The downstream section is maintained subcritical by specifying the water depth as $h = 0.5$ m, the velocity field (u and v) is extrapolated from the domain as described in section 2.3. The water depth at the inflow boundary is extrapolated from the domain, v is set to 0, and u is calculated from the unit discharge, q, as, $u_g = q/h_g$.

Three different values of Manning friction coefficient were used to simulate the transition to steady state. From Fig. 6 (upper-left panel) it can be observed that the solution oscillates less and reaches the steady-state discharge more quickly as the friction factor is increased. The calculated steady state discharge remains constant along the convergent canal and therefore the numerical solution is indeed conservative. To further evaluate the numerical solution, Bernoulli's specific energy equation was used to

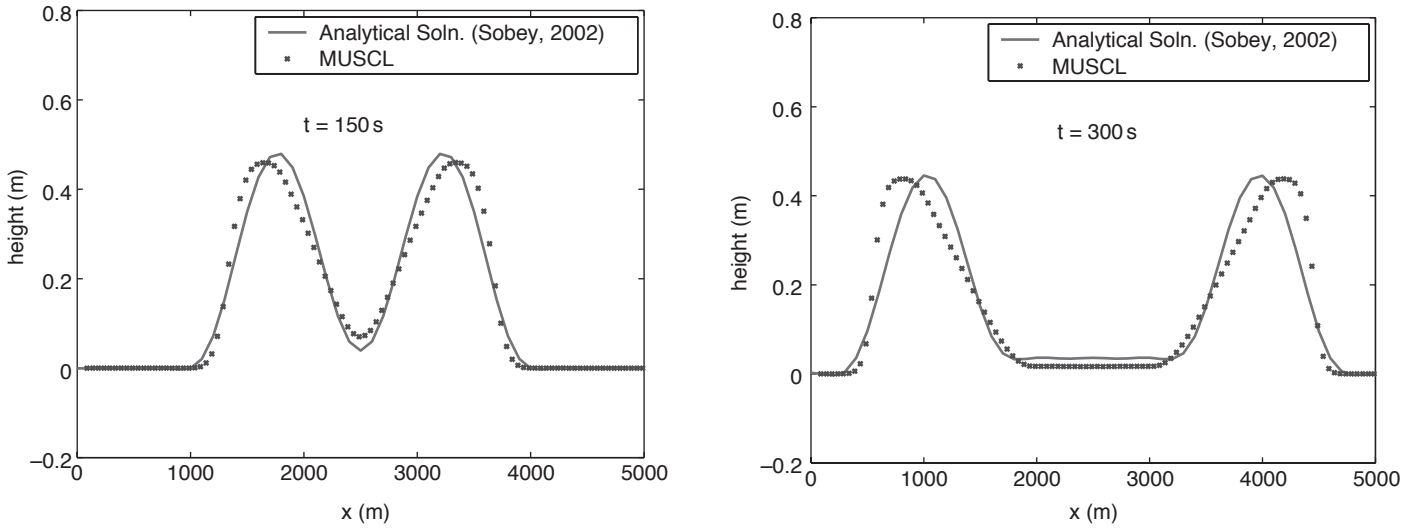

Figure 5 Propagation of positive and negative characteristics along canal at $t = 150$ and 300 s.

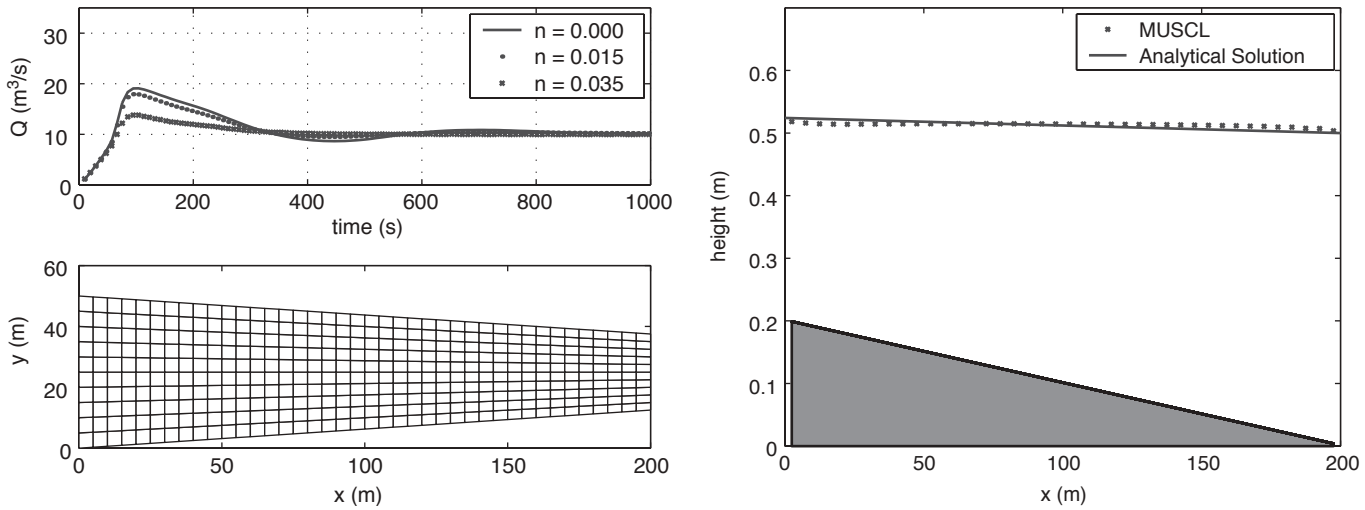

Figure 6 Discretization of convergent canal (lower-left panel). Transition to steady-state outflow discharge given three different values of Manning friction coefficient (upper-left panel). Comparison of water surface height for the MUSCL solution and the Bernoulli equation for the frictionless case in a convergent canal (right panel).

determine the steady state water surface elevation in the convergent canal, given the discharge $Q = 10\,\mathrm{m}^3/\mathrm{s}$ and the downstream boundary condition of $h_b = 0.5\,\mathrm{m}$, assuming an inviscid fluid. The Bernoulli solution was compared with the corresponding frictionless numerical simulation and a satisfactory agreement was found (Fig. 6, right side).

3.4 Hydraulic jump over an obstacle

To evaluate the capacity of the model to simulate transcritical flow, a test problem for flow over a symmetrical bump was used; the problem is similar to a problem presented in Valiani *et al.* (2002). A steady flow of $5\,\mathrm{m}^3/\mathrm{s}$ of a homogeneous fluid with a density of $1000\,\mathrm{kg}/\mathrm{m}^3$, was induced in a rectangular canal 50 m long and 4 m wide, which was discretized into square elements ($\mathrm{d}x = \mathrm{d}y = 1\,\mathrm{m}$). The longitudinal bed profile was given the shape:

$$z_b = \begin{cases} 0.5 - 0.03125(x-28)^2, & \text{for } 24 \le x \le 32\,\mathrm{m} \\ 0, & \text{otherwise} \end{cases} \quad (27)$$

Initially, the water depth was 2.0 m everywhere, while the velocity field was set to zero. The flow in the downstream boundary was maintained subcritical by specifying the water depth as 1.0 m, and the velocity was extrapolated from the domain as described in the above section on Boundary Conditions. The water depth at the inflow boundary was maintained by extrapolating the flow height from the domain. The velocity u was determined as q/h_g, where q is the unitary discharge ($1.25\,\mathrm{m}^3/\mathrm{s/m}$) and h_g is the water surface boundary condition. The analytical comparison is obtained by assuming that Bernoulli's specific energy equation is valid upstream of the hydraulic jump and that the critical depth occurs at the apex of the bump. Downstream from the hydraulic jump, the water surface profile is determined by the downstream boundary condition.

The agreement between the analytical and numerical solution is fairly good (Fig. 7). The simulated shape of the water surface over the bump coincides very well with that given by the analytical solution. Upstream from the obstacle there is a slight difference between the analytical value of the flow depth

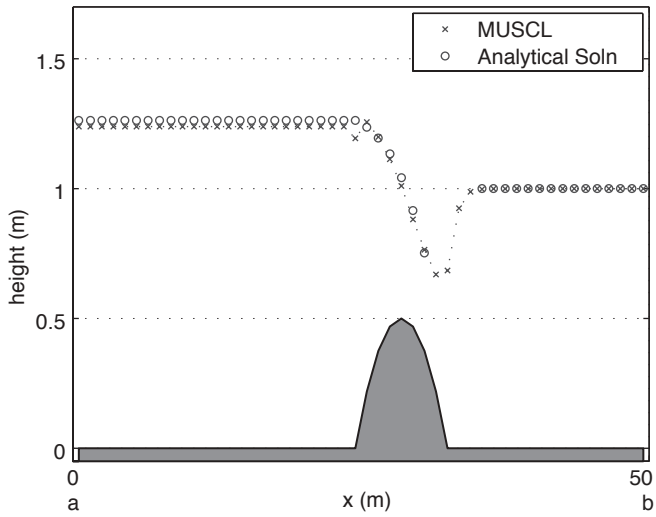

Figure 7 Comparison between the MUSCL solution for the hydraulic jump and the analytical solution given by the conservation of specific energy.

(1.263 m) and that given by the numerical solution (1.238 m). This difference is likely a result of the numerical oscillation that occurs at the beginning of the bump. We argue that the oscillation is due to a simplified (centered difference) integration of the bedslope. Both Bradford and Sanders (2002) and Valiani *et al.* (2002) report inaccuracies resulting from integration of the bedslope; both papers propose more precise techniques for integrating this term.

3.5 Baroclinic circulation at the confluence of two tributaries

To assess the capability of the model to simulate baroclinic residual circulation, an idealized scenario of the confluence of two tributaries was simulated. The confluence was first simulated as two tributaries with the same density, and later as two tributaries with a difference in density between them; the residual circulation is then observed by comparing the time-average of the two scenarios in steady state. The domain is a 15×4 km river reach; discretized into 40×20 FVM cells. Referring to Fig. 8 (top), River 1 enters the reach with a discharge of $Q = 100\,\mathrm{m}^3/\mathrm{s}$, while River 2 enters perpendicular to the flow of River 1 with a discharge of $Q = 20\,\mathrm{m}^3/\mathrm{s}$. The downstream section is affected by a periodic tidal wave of constant amplitude $A = 0.5$ m and period $T = 6$ h. The water velocity and density at the downstream section are extrapolated from the nodes within the domain as described in the section on Boundary Conditions. The bed slope is set to a constant value of 0.0001 from upstream to down, and the simulation was run for a 4-day period to achieve a steady state.

For the first scenario, the density of both rivers was set to $1000\,\mathrm{kg/m}^3$. For the second one, the density of River 1 was set to $1035\,\mathrm{kg/m}^3$, and that of River 2 was set to $1000\,\mathrm{kg/m}^3$. The arrival at steady state can be pinpointed by observing the total water mass, affected by the variable water density, within the domain (Fig. 8, bottom); steady state was achieved at around $t = 2$ days for the second scenario wherein a density difference existed. Evidence of a residual circulation was found by taking

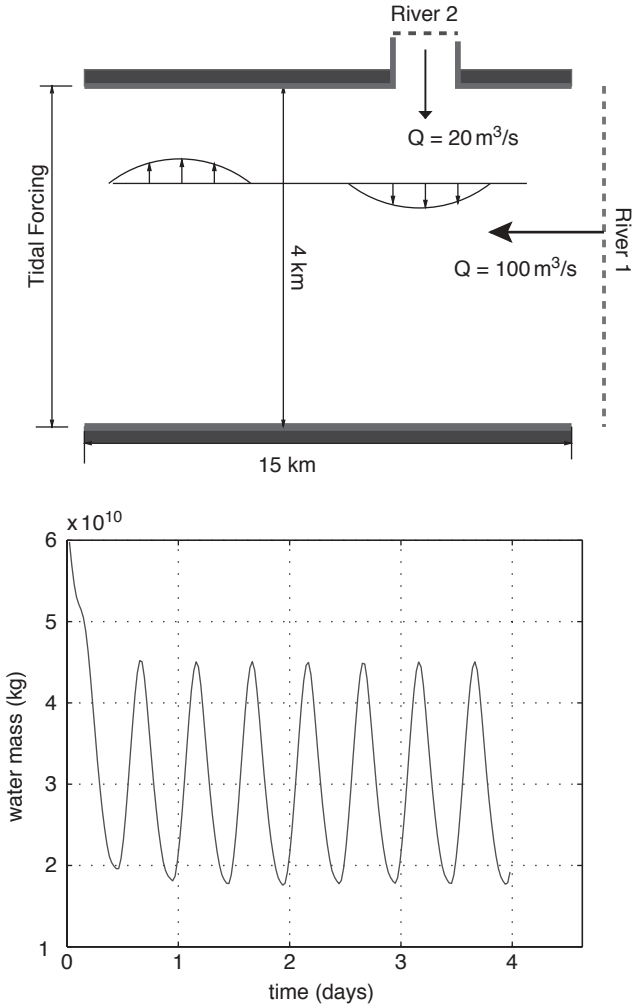

Figure 8 Diagram of the domain and boundary conditions at the confluence of two tributaries with differing density (top). Time variation of the total water mass within the domain of simulation of the confluence (bottom) indicating steady-state.

the time-mean of the transverse velocity (v) over the period of steady state circulation, from days 2 through 4. Figure 9 depicts the transverse velocity for both simulations. In both situations the effect of the inflow of River 2 can be clearly observed. However, a current in the direction opposite to that created by River 2 appears at the downstream end of the domain in the case of tributaries with a density difference (Fig. 9, bottom). This is an example of residual baroclinic circulation induced by the difference in density between the two tributaries.

While this problem is only of qualitative value, as the results of the simulation are not benchmarked against a known solution, it demonstrates the capacity of the model to simulate such residual processes and its potential for accounting for secondary flows even in vertically well-mixed conditions.

4 Río Maipo saline intrusion dynamics

In this section the model is applied to the Río Maipo estuary, in order to establish the basic variability of the saline intrusion and tidal incursion inside the rivermouth. With this aim, a 4-day simulation was carried out using forcing data corresponding to

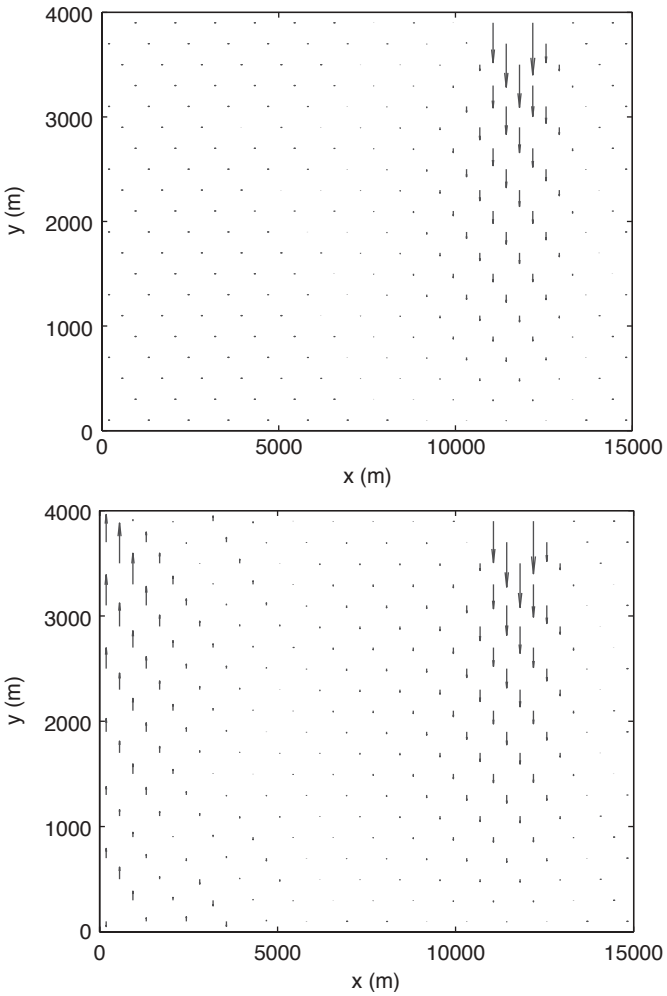

Figure 9 Temporal mean of transverse velocity (v) at the confluence of two tributaries *with* (bottom) a density difference and *without* (top).

time series of tide and freshwater discharges measured in the system during the period of January 2–5, 2000. The predominant morphological feature of the Río Maipo estuary is the littoral sandbar, which restricts flow at the river mouth (Fig. 10). It has

Figure 10 Aerial photograph of Río Maipo estuary; littoral sandbar can be noted at the rivermouth on the left side of the photo. North is oriented upwards.

been observed that during storm events, high flow discharges can generate the partial or complete removal of the sandbar, but that the predominant condition is with the bar present. Field measurements of conductivity within the estuary were taken during June 2001, a period also characterized by the complete presence of the littoral sandbar. These measurements are used as a comparison with the model simulations to assess the general behavior of the flow and salinity intrusion during the presence of the littoral sandbar.

4.1 Field methods

Water samples were collected in the field during a 4-h period on June 23, 2001. The tide was in ebb, with an initial tidal depth of 1.6 m (a.m.s.l.) and a final depth of 0.23 m. Water samples were taken from at least two depths at each measuring station along a longitudinal transect extending from the littoral bar at the river mouth to approximately 2 km upstream. Samples were analyzed for conductivity at the Water Quality Laboratory of the Department of Hydraulic and Environmental Engineering of the Catholic University of Chile. These measurements showed absolutely no vertical stratification in the estuary, validating the depth-averaged approach used by the numerical model. A vertically averaged density was calculated for each measuring station and the resulting longitudinal profile of density in the estuary is plotted in Fig. 11.

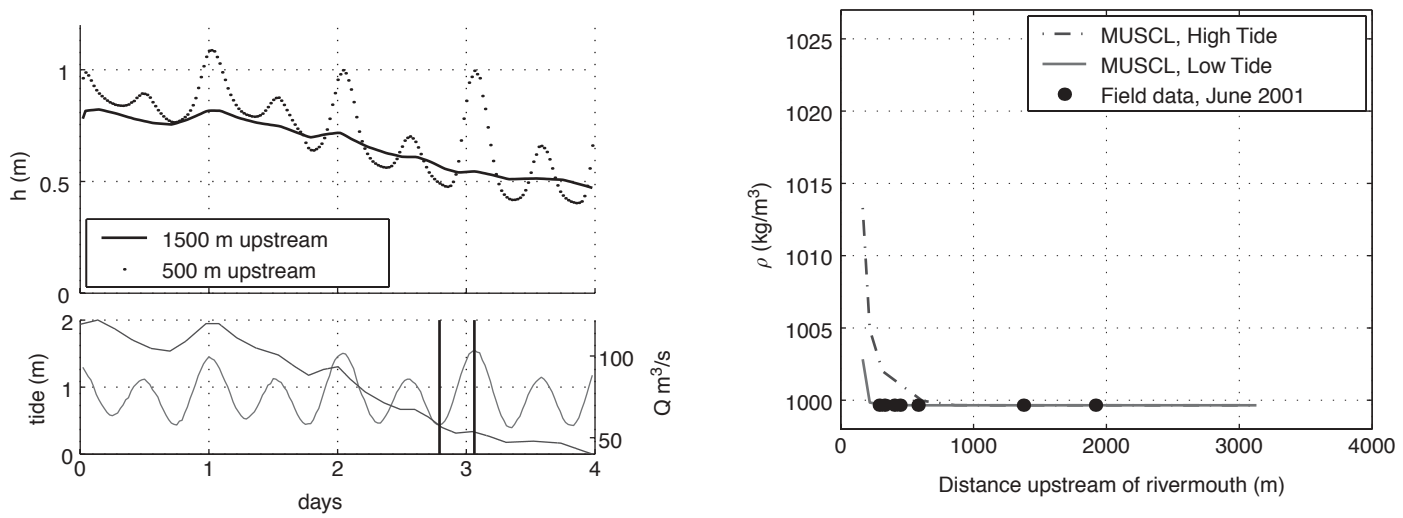

Figure 11 Time series of water height at 500 and 1500 m upstream of the river mouth (upper-left panel), and time series of forcing data, tidal height and river discharge (bottom-left panel). Comparison of measured and simulated longitudinal transects of water density (right panel); both simulated high and low-tide transects are presented. Distances are measured upstream from the river mouth.

4.2 Numerical simulation

The Maipo estuary was discretized into 796 quadrilateral cells, with an average area of 925 m^2, using CUBIT, the mesh generation software developed by Sandia National Laboratory. As no bathymetry data was available at the time of simulation, the flow section was simulated as rectangular. A constant bed slope of 0.0013, which was determined through field measurements, was imposed in the longitudinal direction. The boundary conditions imposed at the inflow boundary correspond to a river type: water height h is extrapolated from the domain, and then used with known discharge data to determine the inflow velocity. Inflow density was set to coincide with freshwater density at 16°C, 999.65 kg/m^3, corresponding with the field measurements. The river mouth boundary condition was imposed using the known tidal height, while velocity was extrapolated from the domain. The water density was set to 1027 kg/m^3, the ambient seawater density. Tidal elevation data was provided by the Chilean Hydrographic and Oceanographic Service (SHOA), and river discharge data was provided by the General Direction of Water Resources (DGA), Ministry of Public Works of Chile.

4.3 Results

The depths of flow depicted in Fig. 11 (upper-left panel) indicate that the tidal incursion reached no further upstream than about 1500 m. At 500 m a clear fluctuation can be noted in phase with the tidal height (indicated in the bottom-left panel, Fig. 11). To compare the results of the simulations with density measurements in the field, longitudinal transects of simulated density were extracted for the extreme high (1.55 m) and low tides (0.43 m) during the 4-day simulation. The transects extend from the rivermouth to 3 km upstream. These transects are compared with the depth-averaged measurements of density taken in the field during ebb tide (Fig. 11, right panel). The instances corresponding to the high and low tide are indicated in the time series of forcing data (Fig. 11, lower-left panel) by vertical bars.

The field measurements show a negligible presence of seawater within the estuary; furthermore the absence of salt 200 m upstream of the rivermouth indicates the presence of a very pronounced density front at the rivermouth. This front is well reproduced by the model and coincides with the field measurements for ebb tide conditions. Given the high current velocities near the rivermouth during the 2001 field trip, water samples were not collected closer than 200 m from the mouth. Simulations indicate that during high tide the density front intrudes further upstream, but the intrusion remains contained within the first kilometer of the estuary (Fig. 11). A notable characteristic of the flow behavior at the rivermouth is that upstream flow, even during flood tide, did not occur during the 4-day simulation. Figure 12 presents two snapshots of the flow velocity at low and high tide, taken from the beginning of day 3 (indicated in Fig. 11, lower-left panel). Despite the relatively low river discharge and the increase in tidal height at the beginning of day 3, the advective transport remains out-of-the-estuary, indicating that the only phenomena capable of generating salt intrusion are related to dispersion mechanisms within the estuary.

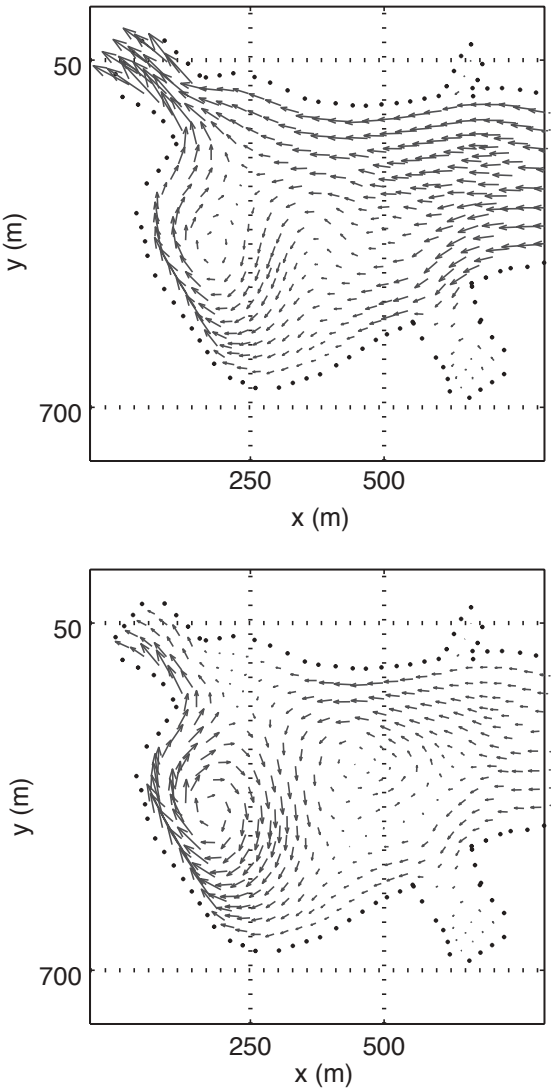

Figure 12 Velocity vectors within the last 800 m of the Maipo estuary. Snapshots correspond to the low (top) and high tide (bottom) instants noted in Fig. 11 by vertical bars (lower-left).

4.4 Discussion

Both simulations and field measurements indicate the surprising conclusion that there is a negligible salinity intrusion within the estuary. A simple 1D analysis of the salt balance in an estuary indicates that the mean longitudinal salinity profile has an exponential decay upstream, with an extension that is proportional to the ratio between the longitudinal dispersion coefficient (D_x) and the mean velocity ($\bar{u}$); that is, $L \propto D_x/\bar{u}$. If L is defined as the distance upstream at which 1% of the seawater salt concentration is found, then L can be determined by $L \approx 5D_x/\bar{u}$. (Fischer, 1979). By using the median value of dispersion coefficients for estuaries presented in Fischer (1979) ($D_x \approx 160\ m^2/s$) and estimating the mean velocity of the estuary as the mean freshwater discharge (90 m^3/s) divided by the mean cross sectional area of the estuary (250 m^2), then the saline intrusion is expected to penetrate approximately 2.2 km upstream. The discrepancy between this analysis and the numerical results is attributed to the presence of the littoral sandbar, which restricts flow and causes elevated flow velocity at the rivermouth. The presence of the sandbar

induces a salt balance that is considerably more dominated by the out-of-estuary advective flow. Thus, during the presence of the sandbar the Río Maipo estuary functions more like a tidal river than an estuary; experiencing the periodic fluctuations of water level driven by the tide, but minimal saline intrusion.

An interesting feature of this system is that the littoral sandbar is removed during extreme floods, with an interval of several years. When the bar is removed the behavior of the system changes dramatically, and this lasts for at least a few months until the bar forms itself all over again. A more complete analysis of the system, including simulations of the Maipo estuary dealing with the abrupt changes resulting from the removal of the littoral bar during a storm occurred in 2002, and results from recent field measurements of flow velocities and salinity in the system will be presented in a subsequent paper.

5 Conclusions

A numerical model has been developed based on recent advances in the shock-capturing numerical methods and applied to a set of shallow-water flow equations with variable-density. The numerical model was tested against several benchmark problems, demonstrating its capacity to reproduce a variety of open-channel flow conditions including the ability to capture abrupt fronts, simulate rapidly varied flow, and reproduce baroclinic residual circulation. The numerical model was applied to simulate flow and salt transport in the Maipo estuary in Central Chile. The numerical results show that the tidal incursion extends approximately 1500 m up-estuary, while the presence of a littoral sandbar affects the flow field, creating a zone of large velocity at the mouth. Advection dominates over dispersion and an abrupt salinity front is created at the river mouth effectively precluding the saline intrusion within the estuary. The simulated density fields agree with field measurements of depth averaged density in the system. Further work will include analysis of the removal of the littoral bar and comparison with recent measurements of velocity fields and salt concentration in the system.

Note: Further information related to this research including model source code and examples is available under Public license from http://www.watersci.org/.

Acknowledgments

Funding for this research was provided by FONDECYT through Project 1010483. The authors would like to thank the Chilean Ministry of Public Works and the Hydrographic and Oceanographic Service of the Chilean Navy for providing the forcing data used in the simulations, and especially Professor Manuel Contreras of the Centre for Applied Ecology and the University of Chile for his generous logistical and informational support.

Notation

A, B = Jacobian matrices of the quasi-linear conservation laws
$\hat{a}$ = Roe-averaged wave celerity
b, b_a, b_b = Top width of the canal in question
$C_{i,j}$ = Centroid of FVM cell i, j
D_x, D_y = Longitudinal and lateral dispersion coefficients
F = Vector of fluxes along the x-axis
$\vec{F}^I$ = Projection of F and G onto each cell face
$F_{\mathrm{AB}}^{\mathrm{adv}}$ = Advective flux perpendicular side AB
$F_{\mathrm{AB}}^{\mathrm{dif}}$ = Diffusive flux perpendicular side AB
G = Vector of fluxes along the y-axis
h = Water surface height above bed
h_g, u_g, v_g, ρ_g = Primitive variables in the fictitious nodes outside the domain boundary
H = Vector of source terms
n = Manning friction coefficient
n = Current time step
$\vec{S}_{\mathrm{AB}}$ = Cell face normal vector for side AB
Δt = Time step between time n and $n+1$
U = Vector of conservative variables
u, v = Flow velocity along x- and y-axis
W = Vector of primitive variables
$\overline{\Delta W}_{i,j}$ = Slope-limited primitive variable
z = Water surface height (from Sobey, 2002a,b)
z_b = Bed height above datum
δ, ω = Eigenvalues of the Jacobian matrices A and B, respectively
ξ, η = Local vector between adjacent $i, i+1$, and $j, j+1$ centroids, respectively
ξ_x, ξ_y = Projection of ξ along x- and y-axis
η_x, η_y = Projection of η along x- and y-axis
κ_{AB} = Vector of the maximum values of λ in cell AB
λ_{AB} = Roe-averaged eigenvalues in cell AB
$\Omega_{i,j}$ = Area of FVM cell i, j
ρ = Variable water density
ρ_0 = Reference water density
τ_{bx} = Longitudinal shear stress
τ_{by} = Lateral shear stress
ζ = Water surface height above datum
γ = Constant friction factor (from Sobey, 2002b)
Δt = Time step between time n and $n+1$

References

1. BRADFORD, S.F. and SANDERS, B. (2002). "Finite-Volume Model for Shallow-Water Flooding of Arbitrary Topography". *J. Hydraul. Engng.* 128(3), 289–298.
2. BRADFORD, S.F. and KATOPODES, N.D. (1999). "Hydrodynamics of Turbid Underflows: Formulation and Numerical Analysis". *J. Hydraul. Engng.* 125(10), 1006–1015.
3. BRADFORD, S.F., KATOPODES, N.D. and PARKER, G. (1997). "Characteristic Analysis of Turbidity Underflows". *J. Hydraul. Engng.* 123(5), 420–431.
4. CHAUDHRY, M.H. (1993). *Open-Channel Flow*. Prentice Hall, Englewood Cliffs, NJ.
5. DYER, K.R. (1997). *Estuaries: A Physical Introduction*, John Wiley and Sons, New York.

6. FISCHER, H.B., LIST, E.J., KOH, R., IMBERGER, J. and BROOKS, N.H. (1979). *Mixing in Inland and Coastal Waters*, Academic Press, London.
7. GROSS, E.S., KOSEFF, J.R. and MONISMITH, S.G. (1999). "Three-Dimensional Salinity Simulations of South San Francisco Bay". *J. Hydraul. Engng.* 125(11), 1199–1209.
8. HIRSCH, C. (1988). *Numerical Computation of Internal and External Flows: Fundamentals of Numerical Discretization*, Vol. 1. John Wiley and Sons, New York.
9. MINGHAM, C. and CAUSON, D.M. (1998). "High-Resolution Finite-Volume Method for Shallow Water Flows". *J. Hydraul. Engng.* 124(6), 605–618.
10. NUJIC, M. (1995). "Efficient Implementation of Non-Oscillatory Schemes for the Computation of Free-Surface Flows". *J. Hydraul. Res.* 33, 101–111.
11. RUIZ-VILLAREAL, M., MONTERO, P., TABEADA, J.J., PREGO, R., LEITAO, P.C. and PÉREZ-VILLAR, V. (2002). "Hydrodynamic Model Study of the Ria de Pontevedra Under Estuarine Conditions". *Est. Coast. Shelf Sci.* 54, 101–113.
12. SANDERS, B.F. and PIASECKI, M. (2002). "Mitigation of Salinity Intrusion in Well-Mixed Estuaries by Optimization of Freshwater Diversion Rates" *J. Hydraul. Engng.* 128(1), 64–77.
13. SANDERS, B.F., GREEN, C., CHU, A. and GRANT, S. (2001), "Case Study: Modeling Tidal Transport of Urban Runoff in Channels Using the Finite-Volume Method". *J. Hydraul. Engng.* 127(10), 795–804.
14. SANDERS, B.F. (2001). "High-Resolution and Non-Oscillatory Solution of the St. Venant Equations in Non-Rectangular Channels Using the Finite-Volume Method". *J. Hydraul. Res.* 39(3), 321–330.
15. SOBEY, R.J. (2002a). "Analytical Solution of Non-Homogeneous Wave Equation". *Coast. Engng.* 44(1), 1–23.
16. SOBEY, R.J. (2002b). "Analytical Solutions for Flood and Tide Codes". *Coast. Engng.* 44(1), 25–51.
17. SLEIGH, P.A., BERZINS, M., GASKILL, P.H. and WRIGHT, N.G. (1998). "An Unstructured Finite-Volume Algorithm for Predicting Flow in Rivers and Estuaries". *Comput. Fluids* 27, 479–508.
18. TORO, E.F. (1997). *Riemann Solvers and Numerical Methods for Fluid Dynamics, A Practical Introduction*. Springer-Verlag, Berlin.
19. TORO, E.F. (2001). *Shock-Capturing Methods for Free-Surface Shallow Flow*. John Wiley and Sons, Chichester, UK.
20. VALIANI, A., CALEFFI, V. and ZANNI, A. (2002). "Case Study: Malpasset Dam-Break Simulation Using a Two-Dimensional Finite Volume Method". *J. Hydraul. Engng.* 128(5), 460–472.
21. ZHAO, D.H., SHEN, H.W., TABOIS III, G.Q., LAI, J.S. and TAN, W.Y. (1994). "Finite-Volume Two-Dimensional Unsteady-Flow Model for River Basins". *J. Hydraul. Engng.* 120(7), 863–883.